NUMERICAL EXPERIMENTS ON WALL TURBULENCE AT LOW REYNOLDS NUMBER

by

Peter LAMMERS, Jovan JOVANOVIĆ, and Franz DURST

A direct numerical simulation of a turbulent channel flow, with regularly spaced two-dimensional roughness elements mounted at the wall and perpendicular to the flow direction, was performed at a very low Reynolds number of $Re \cong 940$ based on the centerline velocity and the full channel height. Using the lattice Boltzmann numerical algorithm, all essential scales were resolved with about $19 \cdot 10^6$ grid points ($1155 \times 129 \times 128$ in the x_1, x_2, and x_3 directions). The computed results confirm the existence of turbulence at such a low Reynolds number. Turbulence persisted over the entire computation time, which was sufficiently long to prove its self-maintenance. By examination of statistical features of the flow across the anisotropy-invariant map, it was found that these coincide with conclusions emerging from the analysis of transition and breakdown to turbulence in a laminar boundary layer exposed to small, statistically stationary, neutrally stable axisymmetric disturbances with the streamwise intensity component (u_1) lower than the intensities in the normal (u_2) and spanwise directions, (u_3), u_1 u_2 u_3. To further support the concept and the results of theoretical considerations of the laminar to turbulent transition process in wall-bounded flows using statistical techniques and to demonstrate its great potential for engineering, an additional simulation was performed of a plane channel flow with regularly spaced riblet elements mounted at the wall and aligned parallel with the flow direction. The supplementary simulation was done at a Reynolds number of Re 6584 using about $250 \cdot 10^6$ grid points ($4096 \times 257 \times 240$). Analysis of the simulation results carried out across the flow region located in the midplane between the riblet elements confirms the central result which lies in the root of the statistical dynamics of the velocity fluctuations in wall-bounded flows: when the velocity fluctuations close to the wall tend towards the one-component state, so that the streamwise intensity component is much larger than the intensities in the normal and spanwise directions, $u_1 \gg u_2$ u_3, the turbulent dissipation rate vanishes at the wall, leading to a significant reduction of the wall shear stress. For the simulated flow case the local value of wall shear stress reduction was found to exceed the wall shear stress reduction $SR \cong 92\%$ which corresponds to a fully developed laminar channel flow with smooth walls at the same Reynolds number.

*Key words: turbulence, flow control, transition*

Introduction

Owing to the very rapid developments in computer technology in the past 20 years, it has become convenient to study turbulent shear flows at low Reynolds numbers by applying numerical techniques. Early work by Deardorff [1] and subsequent contributions of Orszag and Paterson [2], Schumann [3], and Rogallo [4] established basic numerical techniques and computational algorithms for later advanced studies by Kim *et al*. [5], Spalart [6, 7], Gilbert and Kleiser [8], Lyons *et al.* [9], Antonia *et al*. [10], Kuroda *et al*. [11], Eggels *et al*. [12], Choi *et al.* [13], Le and Moin [14], Rogers and Moser [15], and Moser *et al*. [16]. In recent years, it has been obvious that the application of sophisticated numerical algorithms is the only practical way to obtain complete information about flows which is required for understanding the mechanisms that are responsible for the turbulent transport processes. Since numerical simulations of turbulent flows provide full three-dimensional time-dependent velocity and pressure fields, it is expected that these will play the central role in the validation of ideas and concepts that are used in contemporary turbulence research.

Following the early ideas of Reynolds [17] and Taylor [18], who were the founders of statistical fluid mechanics and established basic analytical tools, the statistical theory of transition and breakdown to fully developed turbulence in simple, nearly parallel wall-bounded flows can be worked out proceeding from the basic equations that govern the apparent stresses and by using the closure approximations based on the application of the two-point correlation technique and invariant theory [19, 20]. Conclusions emerging from the theory can be tested by direct comparisons with numerical simulations and experiments. The mechanism responsible for breakdown to turbulence can be identified with a minimum amount of rational input. However, its description might not be digestible for those who reason about transition in a deterministic fashion and exclusively in the physical space where observations usually take place: exposition and use of arguments and resulting deductions may therefore seem shallow, unreasonable, confusing or entirely wrong. If the matter is analyzed in the functional space formed by two scalar invariants which emphasize the anisotropy in the disturbances, the transition problem turns out to be the first one to attack because of its simplicity and specific and unconventional use of arguments then and only then appear logical and transparent. Knowing the mechanism responsible for transition and breakdown to turbulence in advance it was possible to suggest and realize a limited number of *fundamental* simulations with the aim of examining in detail and provide a deep understanding only of those essential features of the transition process that are, in our opinion, of crucial importance for engineering.

The origin of turbulence in wall-bounded flows can be analyzed by looking into the evolution of anisotropy in the Reynolds stresses. The level of the anisotropy of turbulence can be quantified, following ideas of Lumley and Newman [21], using the anisotropy tensor defined as $a_{ij} \quad \overline{u_i u_j} / q^2 \quad (1/3)\delta_{ij}$ (where $q^2 \quad \overline{u_s u_s}$) and its scalar invariants $II_a = a_{ij}a_{ji}$ and $III_a = a_{ij}a_{jk}a_{ki}$. A plot of II_a versus III_a for axisymmetric turbulence, $II_a = (3/2)[(4/3) \ III_a \ ]^{2/3}$, and two-component turbulence, $II_a = (2/9) + 2III_a$, defines the anisotropy-invariant map shown in fig. 1, which according to Lumley [22] bounds all physically realizable turbulence. The two curves in this figure represent

axisymmetric turbulence. The right curve corresponds to turbulence with the streamwise intensity component larger than in the other two directions, u_1 u_3 u_2 ($III_a > 0$), and the left curve corresponds to axisymmetric turbulence with u_1 u_3 u_2 ($III_a < 0$). Along the straight line resides two-component turbulence. The limiting states of turbulence are located at the corner points on the right- and left-hand sides of the anisotropy-invariant map and correspond to one-component turbulence and isotropic two-component turbulence, respectively.

Figure 1 shows the influence of Reynolds number on the anisotropy of turbulence for a channel flow deduced from the databases of direct numerical simulations at low Reynolds numbers. There is a noticeable trend in these data that can be clearly distinguished. With decreasing Reynolds number towards a critical value valid for transition
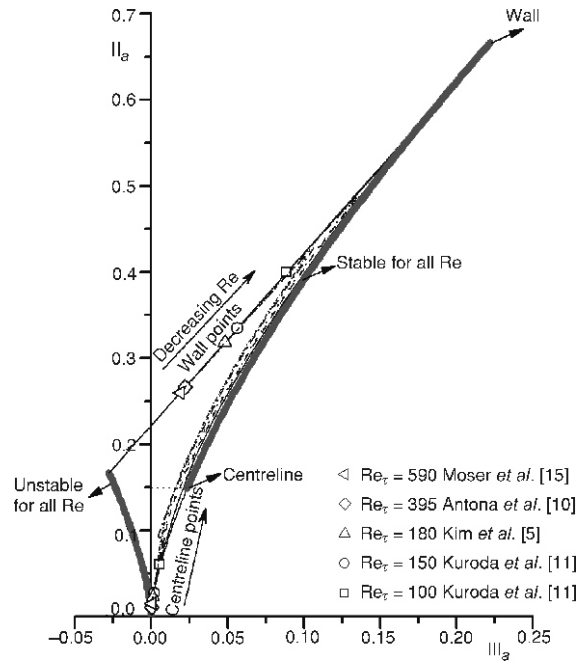
Figure 1. Anisotropy-invariant mapping of turbulence in a plane channel flow at low Reynolds numbers
Data show the trend, as Re Re_{crit}, towards the theoretical solution valid for small, neutrally stable, statistically stationary, axisymmetric disturbances. These disturbances, which are marked with shading, are located at the right boundary of the map. The unstable disturbances, which promote turbulence at very low Reynolds numbers, are located at the left boundary of the map. Note that the trajectory corresponding to the stable disturbances does not coincide with any of well-known solutions emerging from the deterministic theory of the hydrodynamic stability, based on the Orr-Sommerfeld or similar equations, and implies that solutions of these equations can be considered more as an exception than the rule and therefore are expected to be applicable in unusual circumstances

and breakdown to turbulence, the anisotropy increases. Away from the near-wall region, there is tendency for the data to shift towards the right boundary of the anisotropy-invariant map, which corresponds to axisymmetric turbulence (III_a 0). Data that correspond to the region of viscous sublayer and lie along the two-component limit tend towards the one-component turbulence.

The extrapolated trajectory of stable disturbances Re Re_{crit} lies remarkably close to the result of theoretical considerations of the transition process in a laminar boundary layer exposed to small, neutrally stable, statistically stationary, axisymmetric disturbances whose statistical properties are invariant to rotation about the flow direction [23, 24].This particular type of invariance is consistent with the statistical dynamics of the disturbances far away from the near-wall region, which show that u_1 u_3 u_2 [19]. Theoretical considerations, based on the transport equations for the statistical properties of such disturbances, also show that a laminar regime in the boundary layer will persist up to very high Reynolds numbers. In a recent study on the flow development around the airfoil at moderate angle of attack, Jovičić and Breuer [25] were able to animate visually all phases of the transition process from the laminar to a fully developed turbulent state and to show that these coincide with the theoretical predictions shown in fig. 1.

The theoretical analysis of the laminar-turbulent transition process can be extended towards axisymmetric disturbances which lie at the left boundary of the anisotropy-invariant map, III_a 0 (see fig. 1). Analysis of the transport equations for such disturbances leads to the conclusion that these are always unstable and promote very rapid transition and breakdown to turbulence in a laminar boundary layer. These disturbances, however, cannot satisfy the statistical dynamics, which require u_1 u_3 u_2 and therefore are unlikely to appear in the boundary layer at very low Reynolds numbers. In the Appendix we provide a brief review of the theoretical analysis of transition and breakdown to turbulence induced by small axisymmetric disturbances developing in a laminar boundary layer.

The first objective of this work was to examine numerically circumstances which lead to the production and self-maintenance of turbulence at very low Reynolds numbers. In a two-dimensional, plane channel with smooth walls, theoretical considerations, experiments and numerical simulations show that turbulence cannot persist below a certain Reynolds number of about Re 2200 based on full channel height and the centerline velocity.

The authors decided to initiate a numerical program, using a state-of-the-art lattice Boltzmann numerical technique, in order to produce turbulence at very low Reynolds numbers. This was accomplished by placing regularly spaced, two-dimensional roughness elements at the wall in a such way that they are perpendicular to the flow in a plane channel. Such a flow configuration forces turbulence, in the near-wall region, to restructure in a way suggested by theoretical considerations, $(III_a)_{wall} < 0$, in order to promote its generation and self-maintenance at very low Reynolds number.

The second objective was to confirm numerically the central result and the idea of the theoretical investigations of Jovanović and Hillerbrand [26], who examined constraints which led to complete suppression of the velocity fluctuations near the wall. They showed analytically, using only kinematic constraints, that the effective way to damp

36

fluctuations in the near-wall region is to force them to be predominantly one-component (see fig. 1).

For this very special state of wall turbulence, it can be proven analytically and confirmed numerically, using the databases from direct numerical simulations, that the turbulent dissipation rate vanishes at the wall. Under such circumstances, the total energy dissipation rate, which is the rate of conversion of the mechanical energy of flow into heat and which can be evaluated from the work done against the wall shear stress per unit mass of the working fluid, reaches a minimum and a large reduction of the wall shear stress must occur as a logical consequence. The outcome of this work forms a valuable basis for *rational* flow and turbulence control with the aim of preventing laminar to turbulent transition from occurring in the boundary layer at very high Reynolds numbers or of achieving a large drag reduction effect in a fully developed turbulent flow. The results outlined above served as the starting point for identification and successful parameterization of the mechanism responsible for turbulent drag reduction by dilute addition of high polymers by Jovanović *et al*. [27].

In order to produce the desired componentality of the velocity fluctuations leading to the realization of one-component turbulence in the near-wall region, $(II_a)_{wall} \rightarrow 2/3$, the authors performed additional simulation of a plane channel flow with regularly spaced riblet elements mounted at the wall and aligned parallel to the flow direction. For appropriate dimensions of the riblet elements and spacing between them, turbulence in the midplane between the neighboring elements is forced to tend towards the one-component state at the wall. By evaluating the turbulence statistics corresponding only to the plane midway between the riblet elements, it was possible to confirm the results of analytical considerations and to show that, for the state of wall turbulence mentioned above, the turbulent dissipation rate vanishes at the wall, leading to a large reduction of the wall shear stress.

Computational domain

The simulated flow configuration and the employed coordinate system are shown in fig. 2.

For wall-bounded flows, the characteristic scales are defined using the parameters that are available at the wall such as the fluid density ρ, kinematic viscosity of the flow medium ν and shear stress at the wall τ_w. From these parameters emerges the velocity scale u_τ:

$$u_\tau \qquad \sqrt{\frac{\tau_w}{\rho}} \qquad (1)$$

which is related to the streamwise pressure gradient $\partial \overline{P} / \partial x_1$ through the mean momentum equations by:

$$u_\tau \qquad \sqrt{\frac{\delta}{\rho} \frac{\partial \overline{P}}{\partial x_1}} \qquad (2)$$
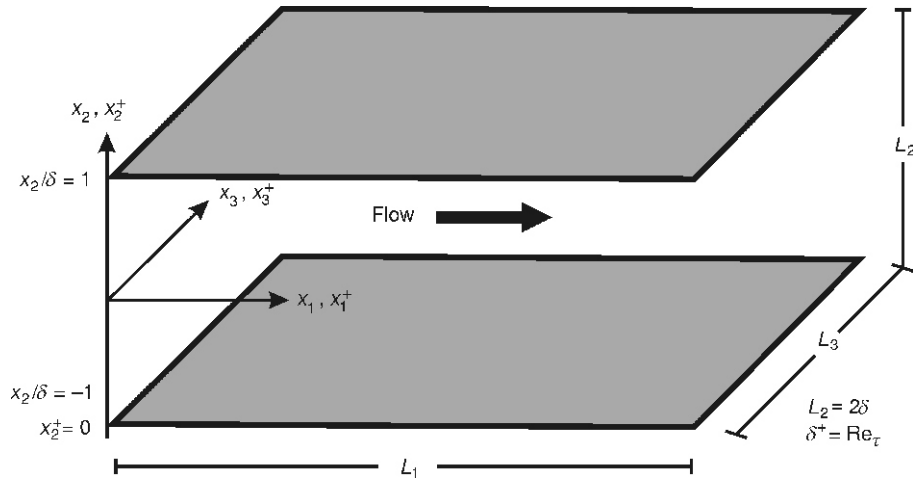
Figure 2. Computational domain of a plane channel flow and coordinate system

where δ is the channel half-width. In terms of the parameters mentioned above, the length scale is defined as $l_\tau = \nu/u_\tau$. Following common practice, all variables are normalized using these inner scales and this is identified in the text by the superscript +, *e. g.* $x^+ = xu_\tau/\nu$.

There are two possibilities for performing numerical simulations of a turbulent channel flow: either to fix the flow rate through the channel or to prescribe the axial pressure gradient and therefore u_τ. For our simulations, we chose the latter option and thereby the Reynolds number Re_τ, based on $\tilde{u}_\tau$ calculated from eq. (2) and the channel half-width, was fixed, for the flow simulation described below, to the value:

$$\mathrm{Re}_\tau \quad \frac{\delta \tilde{u}_\tau}{\nu} \quad \delta \quad 50 \tag{3}$$

In order to simulate the required condition $\mathrm{III}_a < 0$ for the anisotropy of velocity fluctuations close to the wall, which ensures the appearance of turbulence at very low Reynolds numbers, 15 regularly spaced two-dimensional roughness elements were placed at the channel walls and perpendicular to the flow direction. A schematic diagram of the simulated arrangement is shown in fig. 3.

The roughness elements were equally separated by a distance $d^+ \cong 60$ and placed symmetrically, $D^+ = 0$, on both sides of the channel. The non-dimensional height and the width of the roughness elements were h^+ 15 and w^+ 0.78, respectively. For these conditions, the blockage ratio was 30% (defined as the ratio of the area occupied by the roughness element to the cross-sectional area of the channel).

For the geometry shown in fig. 3, the flow is homogeneous in the spanwise direction and quasi-homogeneous in the streamwise direction if the number of roughness elements is sufficiently large. Considering that $N = 15$ satisfies the latter requirement, pe-
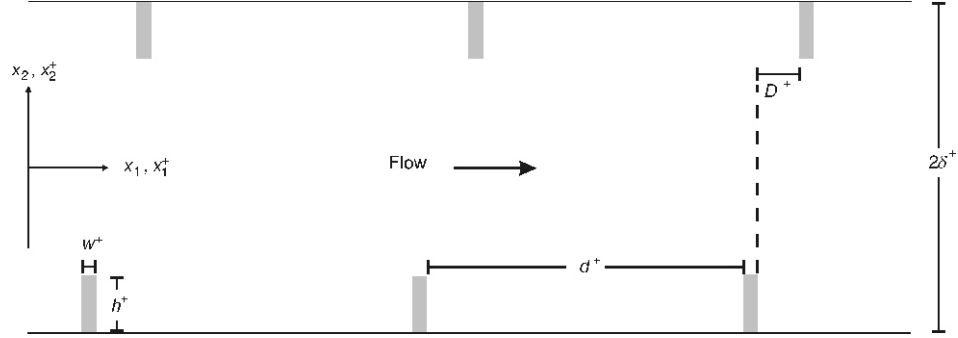
Figure 3. Configuration of the roughness elements mounted at the walls of a plane channel
The elements are extended in the spanwise direction x_3 (see fig. 2). Only part of the computational domain is shown

riodic boundary conditions were used in these directions. Using $1155 \times 129 \times 128$ equidistant Cartesian grids in the x_1, x_2, and x_3 directions, the non-dimensional grid spacing was $\Delta x_i \approx 0.78$.

The adequacy of the spatial resolution of a simulation performed for a configuration with roughness elements is illustrated in fig. 4. These results confirm that the grid
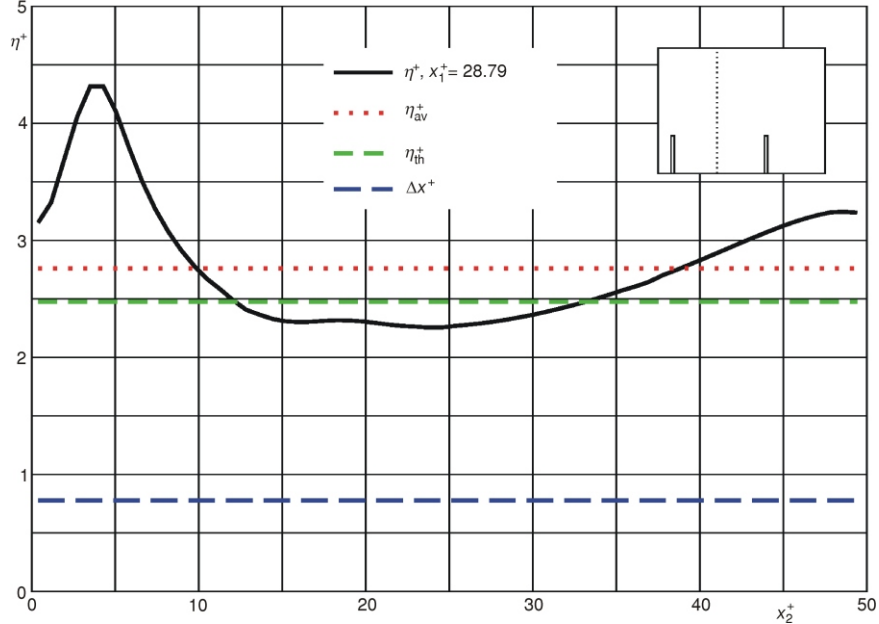

Figure 4. Distribution of the grid (Δx_i) spacing and the local (η^+) and average (η_{av}) Kolmogorov length scale for the channel configuration shown in fig. 3

39

resolution was sufficiently fine to resolve all essential turbulence scales. The estimated value of the Kolmogorov length scale $\eta = (v^3/\varepsilon_h)^{1/4}$ obtained from the average dissipation rate across the channel per unit mass of the working fluid was $\eta_{th} \approx 2.5$ [see Appendix, eq. (23)].

To numerically produce the flow situation leading to realization of one-component turbulence close to the wall, $N = 30$ regularly spaced riblet elements were placed at the channel walls and parallel to the flow direction. Figure 5 shows a schematic representation of the flow field for which simulation was performed for the prescribed value of the Reynolds number:

$$\mathrm{Re}_\tau \approx \frac{\delta \widetilde{u}_\tau}{v} \delta \approx 180 \qquad (4)$$

The riblet elements were equally separated in the spanwise direction by a distance $d^+ \approx 10$ and placed symmetrically on both sides of the channel $D^+ = 0$. The non-dimensional height and the width of the riblet elements were $h^+ \approx 10$ and $w^+ \approx 1.4$, respectively.
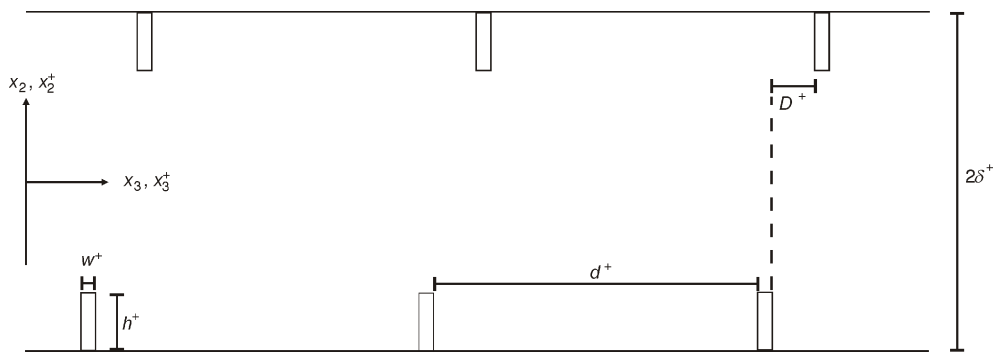
Figure 5. Configuration of a plane channel with riblet elements mounted at the walls
The elements are extended in the streamwise direction x_1 (see fig. 2). Only a small section of the computational domain is displayed

For the geometry shown in fig. 5, simulations were performed by imposing periodic boundary conditions along the streamwise and spanwise directions using $4096 \times 257 \times 240$ equidistant grid points (in the x_1, x_2, and x_3 directions), which corresponds to a non-dimensional grid spacing of $\Delta x_i \approx 1.4$. Figure 6 illustrates the adequacy of the spatial resolution which guarantees that all scales are fully resolved within the computation domain.
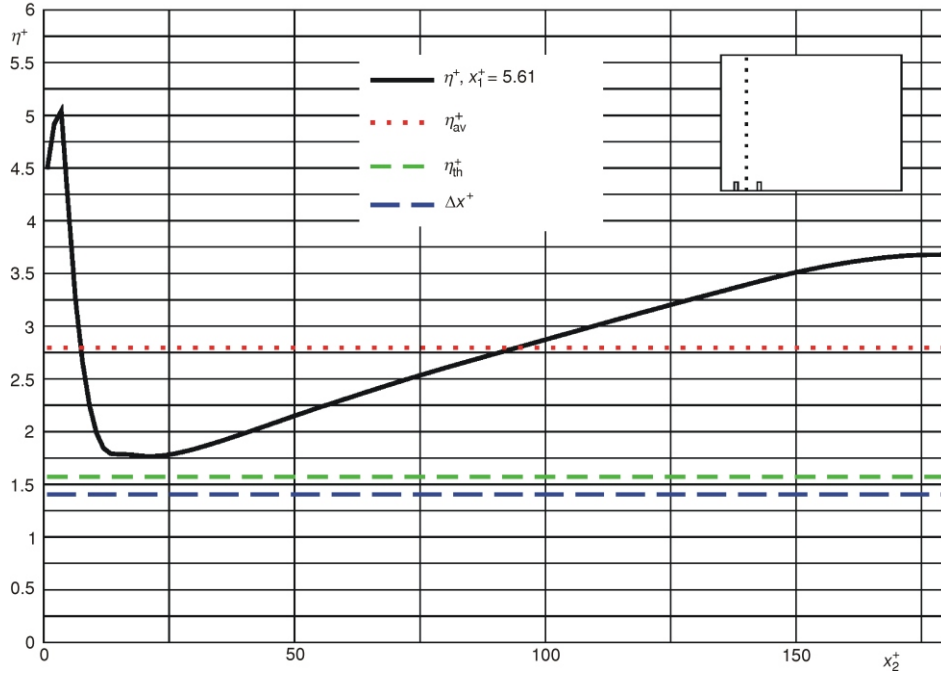
40

Figure 6. Distribution of the grid spacing (Δx_i) and the local (η^+) and average (η_{av}) Kolmogorov length scale for the channel configuration shown in fig. 5

Numerical method

The choice of the numerical method was motivated by the demand for an algorithm with small computing costs per grid point and time step. Owing to the complicated geometry, the lattice Boltzmann method (LBM) was a logical and attractive choice and will be briefly described. Further details about the history and theory of this computational technique can be found in review articles by Benzi *et al.* [28] and Chen and Doolen [29] or in the books by Wolf-Gladrow [30] and Succi [31].

The LBM method was developed during the last 10 years as an alternative approach to existing methods of computational fluid dynamics (CFD). The method utilizes the fact that information on the velocity $\vec{U}$ and the pressure p of a viscous fluid can be obtained by solving a kinetic equation for a one-particle distribution function f instead of Navier-Stokes equations directly. The function $\tilde{f}$ $\tilde{f}(\vec{\xi}, \vec{\rho}, \tau)$ depends on the molecular velocity $\vec{\xi}$, the position in space $\vec{r}$ and the time $\tilde{t}$. The hydrodynamic quantities are obtained from the moments of the distribution function.

A very popular kinetic model is described by the Boltzmann equation together with the so-called Bhatnagar-Gross-Krook (BGK) ansatz [32] for the collision operator:

$$(\partial_{\tilde{t}} + \vec{\xi} \cdot \vec{\nabla}_r + \vec{F} \cdot \vec{\nabla}_{\vec{\xi}})\widetilde{f}(\vec{\xi},\vec{r},\tilde{t}) = -\frac{\widetilde{f}(\vec{\xi},\vec{r},\tilde{t}) - \widetilde{f}^{eq}(\vec{\xi},\vec{r},\tilde{t})}{\lambda} \qquad (5)$$

where $\vec{F}$ is the external force. The function $\widetilde{f}^{eq}$ corresponds to the equilibrium (Maxwell-Boltzmann) distribution and λ is a relaxation time. This equation is discretized in time and space. Additionally, a finite set of velocities $\vec{c}_i$ for $\vec{\xi}$ has to be defined. As a result of discretization, the following non-dimensional equation is obtained:

$$f_i(\vec{x}+\vec{c}_i, t+1) - f_i(\vec{x},t) = -\omega[f_i(\vec{x},t) - f_i^{eq}(\rho,\vec{U}+\frac{\vec{\varepsilon}}{2\rho},\vec{x},t)] + 3t_p\frac{2-\omega}{2}\vec{c}_i \cdot \vec{\varepsilon} \qquad (6)$$

where f_i is the distribution function of the velocity $\vec{c}_i$. A detailed derivation of how the lattice Boltzmann equation recovers the Navier-Stokes equation can be found in [33] and especially for eq. (6) in [34].

Equation (6) appears to be a first-order scheme but is in fact second order in time [35]. Without loss of generality we may choose $\delta t = 1$ for the time step and $\rho = 1$ for the density. The force density $\vec{\varepsilon}$ is given by the pressure gradient according to $\vec{\varepsilon} = -\vec{\nabla}p$, whereby ε_1 is the only remaining component in our case. The macroscopic behavior of eq. (6) is obtained by a Chapman-Enskog procedure [36] together with a Taylor expansion of the Maxwell-Boltzmann equilibrium distribution for small velocity (small Mach number). For this equilibrium distribution:

$$f_i^{eq} = t_p\rho[1 + \frac{c_{i_\alpha}U_\alpha}{c_s^2} + \frac{U_\alpha U_\beta}{2c_s^2}(\frac{c_{i_\alpha}c_{i_\beta}}{c_s^2} - \delta_{\alpha\beta})] \qquad (7)$$

it can be shown that the Mach number must be $|u/c_s| \ll 1$ in order to satisfy the incompressible Navier-Stokes equations. The parameters t_p and $p = \|\vec{c}_i\|^2$ depend on the discretization of the molecular velocity space. Various models can be found in [37]. For the present simulation a three-dimensional model with 19 velocities $\vec{c}_i$, $i = 0, ..., 18$ (D3Q19) was employed. The D3Q19 model has the parameters $t_0 = 1/3$, $t_1 = 1/18$, and $t_2 = 1/36$. A sketch of $\vec{c}_i$ is given in fig. 7. From the Chapman-Enskog procedure the expression for the viscosity ν in terms of the relaxation parameter ω follows as $\nu = (1/6)[(2/\omega) - 1]$.

The most commonly used condition to implement solid walls in the LBM is the so called bounce-back rule. This rule forces the populations leaving the computational domain to return to the node of departure with the opposite velocity. This rule is very simple and enforces mass conservation. Here it is implemented in such a way that the solid boundaries are placed half way between two nodes. This is referred to in the literature as a bounce-back on the link (BBL). It has been shown that the BBL scheme gives second--order accurate results for plane boundaries [38]. In combination with he marker-and-cell approach, even geometries much more complex than plane walls can be matched to the

42

grid. This explains the popularity of the method for studying porous media or equivalent flow problems [39]. The bounce-back rule is also used for treatment of the flow close to the solid boundaries in present.

Our implementation of LBM is validated against the pseudo-spectral simulation of Kim *et al*. [5] for plane channel flow at Re_τ 180. Figure 8 shows that profiles of the mean velocity, root-mean-square velocity fluctuations, turbulent shear stress $\overline{u_1 u_2}$ and the balance of the energy ($k = q^2/2$) equation agree closely with the results of the study mentioned above. Figure 9 displays the isosurface of the instantaneous vorticity which visually illustrates the development of typical flow structures in
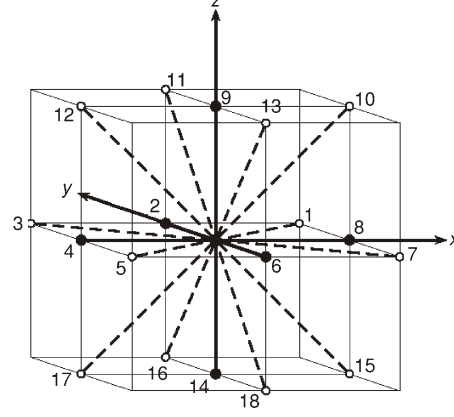

Figure 7. Lattice geometry and the velocity vectors $\vec{c}_i$ for the three-dimensional 19--velocity D3Q19 model
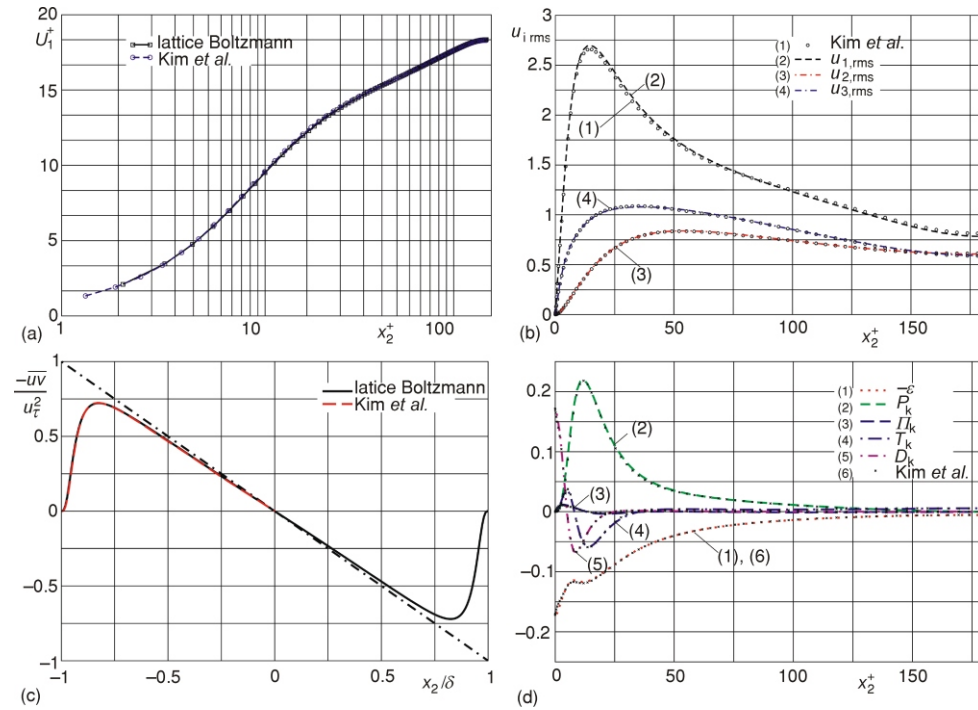
Figure 8. Comparison of a lattice Boltzmann and a pseudo-spectral simulation of Kim *et al*. [5] for a plane channel flow at Re_τ 180. Non-dimensionalized profiles of: (a) mean velocity, (b) rootmean-square velocity fluctuations, (c) turbulent shear stress $\overline{u_1 u_2}$, and (d) the balance of the *k* equation all scaled on the inner variables

wall-bounded turbulent flows. It is worth noting that the results displayed in figs. 8 and 9 were obtained with a grid size of 4096 257 256, resulting in a resolution Δx_i 1.4. This resolution is nearly twice as coarse as that for the simulation performed for a channel configuration with the roughness elements.
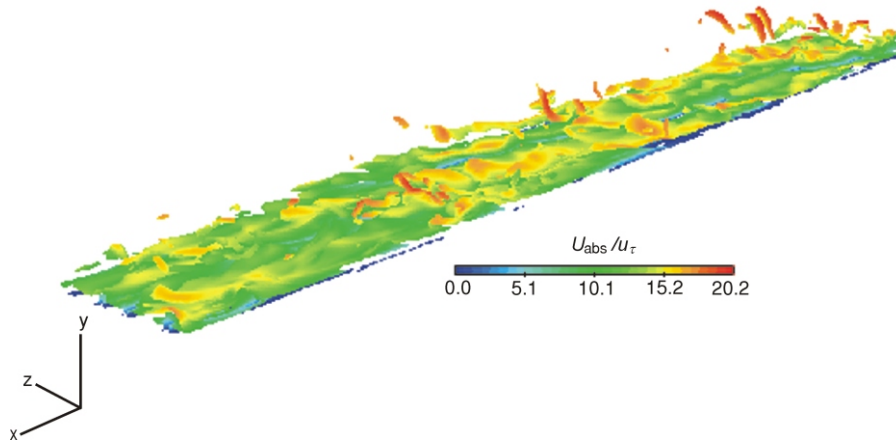
Figure 9. Isosurface of instantaneous vorticity $|\vec{\nabla} \times \vec{U}|/(u_\tau^2/\nu)$ 0.4 scaled on the inner variables for a plane channel flow at Re_τ 180 (color image see on our web site)

For all simulations reported in this paper, an initial field was generated by a superposition of the universal velocity distribution $\vec{u}_0$ and perturbation produced by a periodic array of eddies according to:

$$
\vec{v}_0 = \vec{u}_0 + A (x_{3_1}^c - x_3) \exp\left[-\frac{[(x_2 - x_{2_1}^c)^2 + (x_3 - x_{3_1}^c)^2]}{(R)^2}\right]
$$

$$
\underbrace{(x_2 - x_{2_1}^c)}_{\text{streamwise}}
$$

$$
(x_{2_i}^c - x_2)
$$

$$
+ B \sum_{i=2}^{N_c-1} (x_1 - x_{1_i}^c) \exp\left[-\frac{[(x_1 - x_{1_i}^c)^2 + (x_2 - x_{2_1}^c)^2]}{(R)^2}\right] \tag{8}
$$

$$
\underbrace{0}_{\text{spanwise}}
$$

Although the exponential functions violate the incompressibility condition, they serve to damp the amplitude of the eddies near the wall and avoid stability problems during the initial phase of the simulation. In the present simulation, the constants in the universal velocity distribution:

$$\frac{\overline{U}_1}{u_\tau} \quad \frac{1}{\kappa} \ln \frac{x_2 u_\tau}{\nu} \quad C \tag{9}$$

were chosen as $\kappa = 0.4$ and $C = 5.2$. The other parameters involved in eq. (8) were set to $A^+ \quad 0.07, B^+ \quad 0.14$, and $N_c = 8$. The initial velocity field corresponds to a finite array of periodic spanwise eddies with centers along a line parallel to the x_1 axis and one streamwise eddy centering in the middle of the x_2-x_3 plane. The center of the first spanwise eddy was located at $x_{1_i}^c \quad \delta$ from the inflow boundary and the rest of the eddies were separated at regular intervals of $2\delta^+$.

Results

Experiments with surface-mounted roughness elements

Starting from the initial field, governing equations were integrated until the flow reached a statistically steady-state. This state could be identified by monitoring running averages of the turbulence statistics very close to the wall and at the channel centerline.

Figure 10 shows that the relative turbulence intensity converges to about 40% close to the wall and 10% at the channel centerline, which is consistent with the data measured by Fischer, Jovanović and Durst [40] in a fully developed turbulent channel flow at low Reynolds numbers. When the statistically steady state had been reached, the equations were further integrated in order to prove self-maintenance of turbulence over a sufficiently long interval of time and to increase the statistical sample for the evaluation of various correlations of interest. Calculations of the plane channel flow with smooth walls


Figure 10. Relative turbulence intensity at two monitoring locations close to the wall and at the channel centerline as a function of normalized time $\tau = t/(\delta/u_\tau)$ of integration. These results confirm the persistence and self-maintenance of turbulence over more than 6000 integral time-scales of the flow
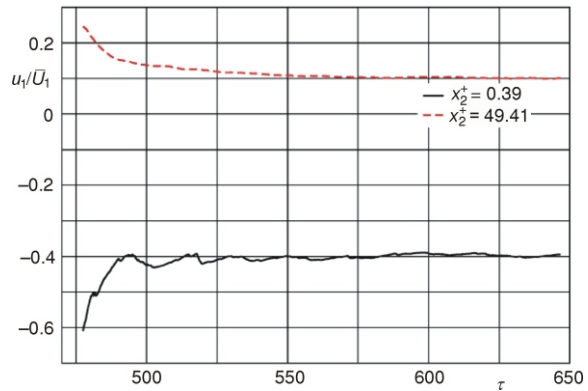
starting from identical initial and boundary conditions yielded a laminar flow field after very few integration time steps.

Mean flow

After the simulations had reached a statistically steady-state, the mean flow properties were calculated by averaging instantaneous flow fields over time and also over the vertical planes along the gap between two neighboring roughness elements. For large numbers of symmetrically arranged and regularly spaced roughness elements, such averaging is permitted since the mean flow is expected to be symmetrical and quasi-periodic in the streamwise direction. This specific type of time and space averaging allowed a considerable increase in the sample for the determination of turbulence statistics.
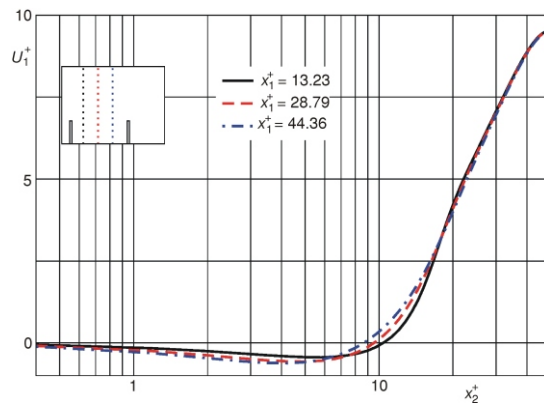
Figure 11. Normalized mean velocity profiles in the flow direction

The profiles of the mean velocity in flow direction for three cross-sections between the roughness elements are shown in fig. 11. These data are non-dimensionalized by the wall friction velocity $\overline{U}_1$ $\overline{U}_1/\tilde{u}_\tau$ calculated from the pressure gradient along the channel using eq. (2) and plotted *vs.* the normalized distance from the wall x_2 $x_2\tilde{u}_\tau/\nu$. The self-similarity of these profiles in inner scaling implies that the flow is dominated entirely by the condition at the wall. The flow in the near-wall region is very weak and shows clear signs of reversal. The reversed flow occupies the entire gap between the two roughness elements. The data in fig. 11 show that the computed results correspond to a Reynolds number of:

$$\mathrm{Re}_c \quad \frac{2\delta\overline{U}_c}{\nu} \quad 940 \tag{10}$$

based on the full channel height (2δ) and the mean centerline velocity ($\overline{U}_c$).

Turbulence statistics

The profiles of all three turbulence intensity components u_i $(u_i^2)^{1/2}, i = 1, 2, 3$, normalized with $\tilde{u}_\tau$ are shown in fig. 12. The collapse of these profiles is not as good as
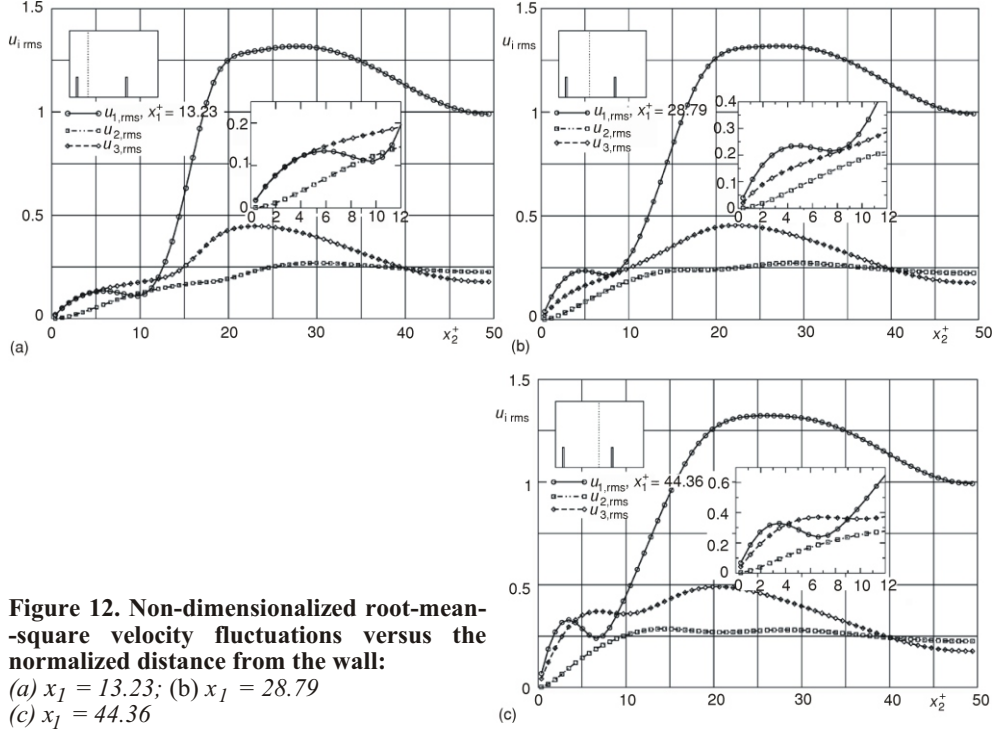
**Figure 12. Non-dimensionalized root-mean-
-square velocity fluctuations versus the
normalized distance from the wall:**
(a) x₁ = 13.23; (b) *x₁ = 28.79*
(c) x₁ = 44.36

for the mean flow, shown in fig. 11, but the displayed data show that the fluctuating velocity components are reasonably correlated with $\widetilde{u}_\tau$ across the entire flow field. The general shape of these profiles differs considerably from those of the smooth channel shown in fig. 8. The maximum of turbulent intensity is shifted away from the near-wall region and the intensities of normal and spanwise velocity components are lower than for turbulence developing along the smooth boundaries.

In close proximity to the wall, turbulence undergoes considerable modification owing to the presence of the surface roughness. Roughness elements partially inhibit motions in the streamwise direction, which result in comparable growth of the streamwise u_1 and the lateral u_3 intensity components. Since the presence of the solid boundary suppresses heavily motions in the direction normal to the wall (u_2 0), fluctuations are forced to restructure from the stable state located at the one-component limit towards the unstable state which is around the isotropic two-component limit (see fig. 1).

Figure 13 shows traces of the joint variations of the invariants II_a and III_a of a_{ij} across the anisotropy-invariant map. This figure indicates that roughness elements force the anisotropy very close to the wall to decrease. As a consequence, the invariants, which lie along the two-component state, shift towards the left corner of the anisotropy map, which corresponds to the isotropic two-component turbulence.
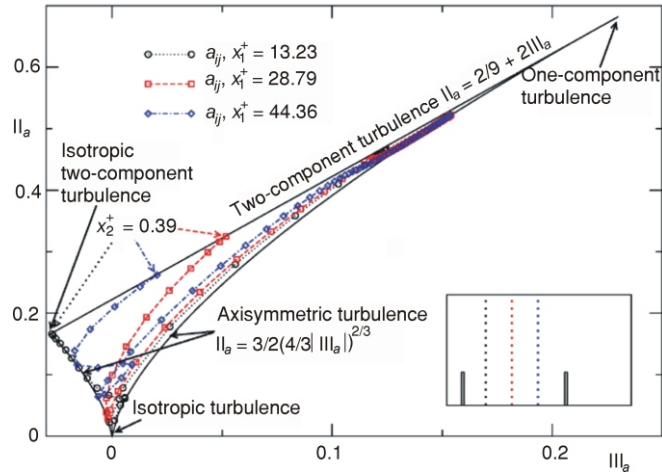
Figure 13. Development of turbulence across the aniso-tropy-invariant map
The trend in the simulation data near the wall indicates a tendency towards the isotropic two-component limit
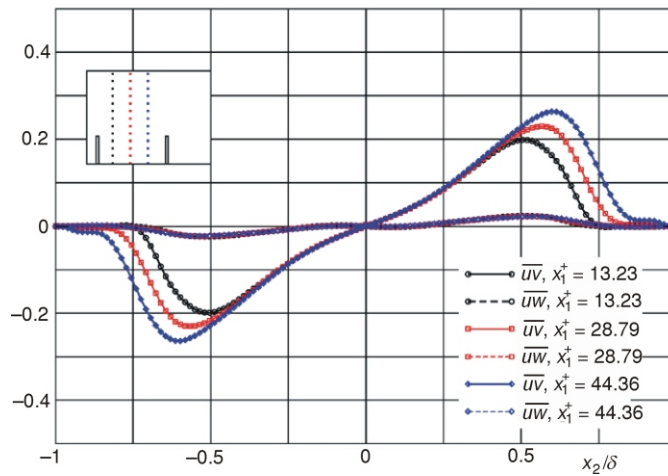
Figure 14. Turbulent shear stresses $\overline{u_1 u_2}$ and $\overline{u_1 u_3}$ non-dimensionalized with $\tilde{u}_\tau$ vs. the normalized distance from the wall

The turbulent shear stress profiles normalized in inner scaling are shown in fig. 14. Owing to the broken homogeneity in the streamwise direction due to the presence of

the roughness elements, apart from $\overline{u_1 u_2}$, additional shear stress $\overline{u_1 u_3}$ exists which is, however, very small. The computed profiles of $\overline{u_1 u_2}$ reveal that it is negligible across the entire region separated between the roughness elements. In the region above the roughness elements $\overline{u_1 u_2}$ shows a linear rise up to the channel centerline. This behavior of $\overline{u_1 u_2}$ is similar to the shear stress development in a channel flow with smooth walls, shown in fig. 8, with the difference, however, that the overall level is much lower.

The balance of the equation which governs the turbulent kinetic energy:

$$\underbrace{\frac{\partial k}{\partial t} \quad \overline{U}_k \frac{\partial k}{\partial x_k}}_{\mathrm{D}k/\mathrm{D}t} \quad \underbrace{\overline{u_i u_k} \frac{\partial \overline{U}_i}{\partial x_k}}_{P_k} \quad \underbrace{\nu \overline{\frac{\partial u_i}{\partial x_k} \frac{\partial u_i}{\partial x_k}}}_{\varepsilon} \quad \underbrace{\frac{1}{2} \frac{\partial \overline{u_s u_s u_k}}{\partial x_k}}_{T_k} \quad \underbrace{\frac{1}{\rho} \frac{\partial \overline{p u_k}}{\partial x_k}}_{\Pi_k} \quad \underbrace{\nu \frac{\partial^2 k}{\partial x_k \, \partial x_k}}_{D_k} \quad (11)$$

is shown in fig. 15. All terms which contribute to the balance of the k equation, convection $\mathrm{D}k/\mathrm{D}t$, production P_k, turbulent transport T_k, pressure transport Π_k, viscous dissipation ε, and the viscous diffusion D_k, are scaled with inner variables. The computed
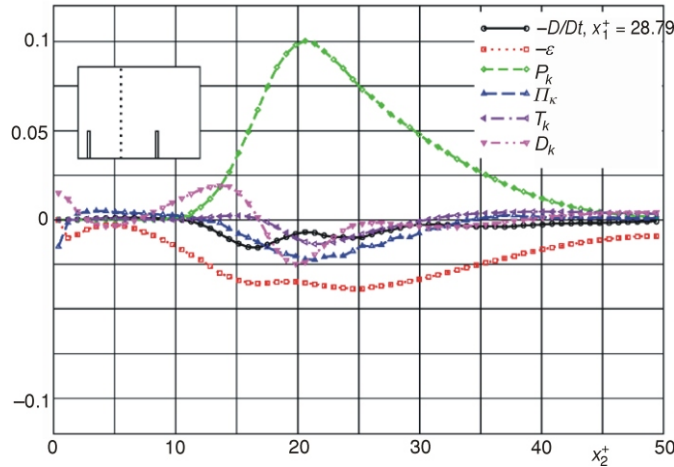
Figure 15. Terms conributing to the balance of the energy k equation normalized by $\tilde{u}_\tau^4/\nu^2$

data show that the production and the viscous dissipation processes are dominant in the balance of k. These two processes are, however, out of equilibrium across the entire flow field. In the region between the roughness elements, only the dissipation process is active and is balanced by the viscous diffusion. In the outer flow, above the roughness elements, the production process is dominant in the budget of the k equation and is balanced partially by the dissipation and to a larger extent by other processes of transport nature.
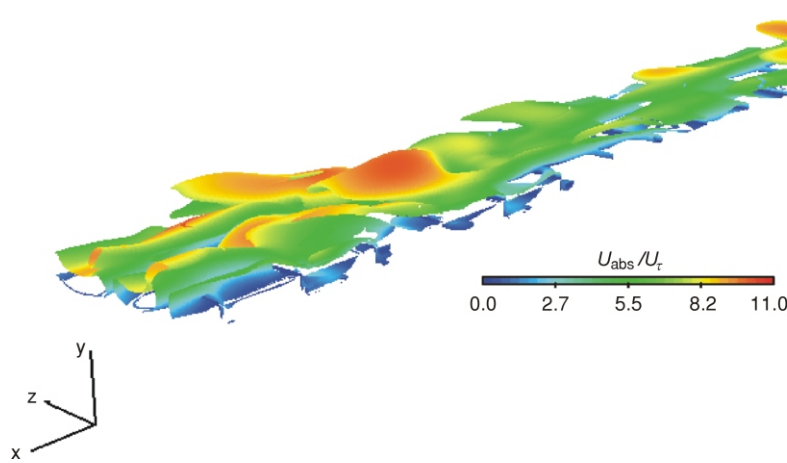
Figure 16. Isosurface of vorticity $\left|\vec{\nabla} \times \vec{U}\right| / (\tilde{u}_\tau^2 / \nu) \approx 0.4$ **for the configuration shown in fig. 3 and Re$_t \approx$ 50, $\tau \approx$ 600 (color image see on our web site)**

Figure 16 shows the isosurface of the instantaneous vorticity across the entire flow domain scaled on the inner variables. This form of flow visualization illustrates qualitative features of turbulence at very low Reynolds number: formation of relatively large, quasi-periodic, weakly disordered structures elongated in the streamwise direction with small spread of scales. This pattern differs from similar structural information shown in fig. 9 for a plane channel flow developing along smooth walls.

Experiments with surface-mounted riblet elements

In this section, we turn attention to the analysis of the simulation results carried out for the channel flow with riblet elements. The analysis to be presented is restricted only to the midplane between the elements where turbulence is forced to reach the one-component limit at the wall. Examination of the statistical properties of such turbulence provides the possibility not only of verifying the theoretical considerations of Jovanović and Hillerbrand [26], but also of demonstrating that these considerations are directly related to the chief mechanism of wall shear stress reduction in turbulent wall-bounded flows.

Mean flow

Figure 17 shows mean velocity profiles in the channel with smooth and with riblet walls normalized with wall friction velocities u_τ and $\tilde{u}_\tau$ calculated from the pressure gradient along the channel using eq. (2). The data displayed in this figure show that the computed results correspond to a Reynolds number of:

50

$$\mathrm{Re}_c \quad \frac{2\delta \overline{U}_c}{\nu} \quad 6584 \tag{12}$$

based on the full channel height and the mean centerline velocity.

Since the Reynolds numbers and the pressure drops for simulated flows with and without riblets are almost identical, we conclude from fig. 17, by taking into account the threefold increase in the wetted surface area, that riblet elements greatly reduce the wall shear stress τ_w and that the average wall shear stress reduction (SR) defined as:

$$SR \quad 1 \quad \frac{(\tau_w)_{\text{riblet}}}{(\tau_w)_{\text{smooth}}} \tag{13}$$

is about $\overline{SR}$ 66%.
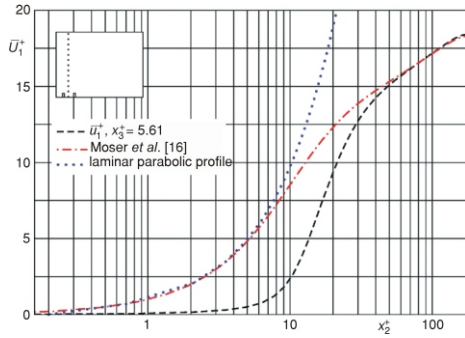
Figure 17. Normalized mean velocity profiles in a plane channel with smooth walls and in the flow region located in a midplane between the riblet elements
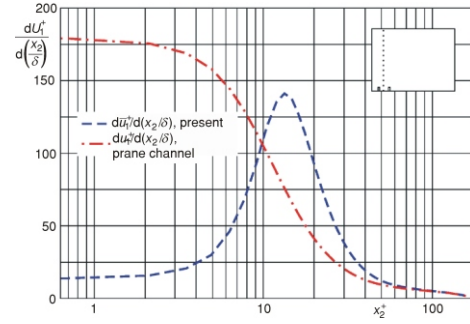
Figure 18. Normalized mean velocity gradients in a plane channel with smooth walls and for the flow region located in a midplane between the riblet elements

Profiles of the mean velocity gradients shown in fig. 18 reveal a dramatic reduction in the wall shear stress in the midplane between the riblet elements. The data presented in this figure suggest that the local value of SR:

$$(SR)_{\text{mid.}} \quad 1 \quad \frac{(\tau_{\text{w}})_{\text{riblet}}^{\text{midplane}}}{(\tau_{\text{w}})_{\text{smooth}}} \tag{14}$$

is $(SR)_{\text{mid.}}$ 92% and exceeds the value:

$$(SR)_{\text{lam.}} \quad 1 \quad \frac{(\tau_w)_{\text{smooth}}^{\text{laminar}}}{(\tau_w)_{\text{smooth}}^{\text{turbulent}}} \tag{15}$$

$(SR)_{\text{lam.}}$ 85%, which corresponds to a fully developed laminar channel flow with smooth walls at the same Reynolds number (see [13]).

Turbulence statistics
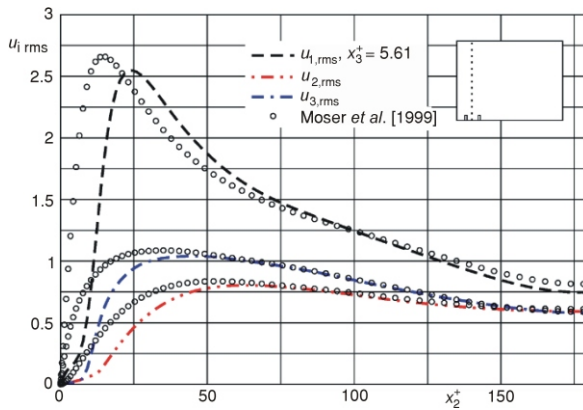
Figure 19. Non-dimensionalized root-mean-square of the velocity fluctuations *vs.* normalized distance from the wall for the smooth channel and in the midplane between the riblet elements

Figure 19 provides a demonstration for modifications of turbulence induced by the presence of the riblet elements. The data presented correspond to the flow region in the midplane between the riblet elements and are normalized with the wall friction velocity calculated from eq. (2).

The displayed profiles of the intensity components suggest that the principal mechanism of turbulence modification is associated with the ability of the riblets to delay the growth of turbulence in the region adjacent to the wall. Near the wall the lateral intensity component is suppressed by the riblets and forced to follow the trend of the intensity component perpendicular to the wall. Such behavior of the turbulent stresses implies that these will assume a form as in axisymmetric turbulence and tend towards the one-component limit at the wall. Away from the wall region, turbulent intensities follow a similar pattern common for flows developing along smooth boundaries.

For the channel configuration with the riblet elements, the simulated database provided the opportunity to examine the evolution of turbulence across the anisotropy-invariant map and confirm the theoretical deduction that an increase in anisotropy near the wall is associated with a significant decrease in the wall shear stress. The results of these considerations are illustrated in fig. 20. In the midplane between the riblet elements, anisotropy is greatly increased in the viscous sublayer in comparison to the corresponding flow region of a fully developed channel flow (see fig. 20b). For the simulated geometry and arrangement of the riblet elements, turbulence in the midplane between the riblets reaches the one-component state at the wall. Simulation results show that the anisotropy is only marginally altered at the tip of the riblets in comparison with the level which the anisotropy attains in the viscous sublayer of a turbulent flow developing along smooth boundaries (see fig. 20a). Away form the near-wall region, the evolution of anisotropy follows similar trends in magnitude and character as in a fully developed plane channel flow.

The discussed behavior of turbulence in the near-wall covered with riblets is reflected in the distribution of the turbulent dissipation rate which is presented in fig. 21. Owing to ability of riblets to significantly damp near-wall turbulence in the midplane between
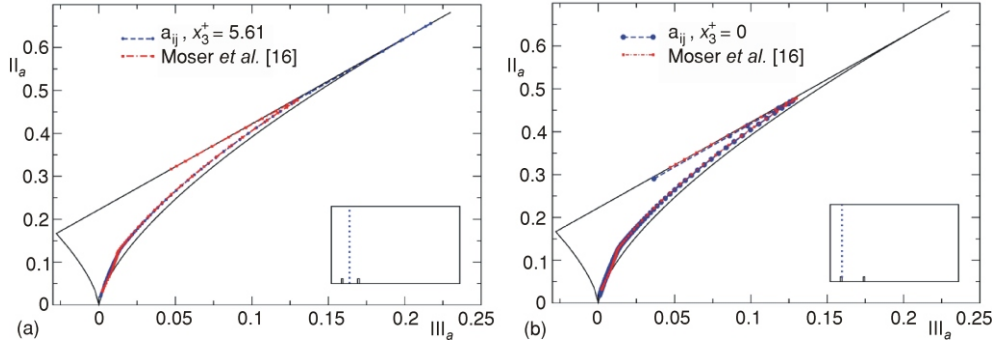
Figure 20. Anisotropy invariant mapping of turbulence in a channel flow with the riblet elements: (a) above the riblet; (b) in the plane between the riblet elements

them, the turbulent dissipation rate vanishes at the wall instead of reaching its maximum as in flows developing along smooth walls. Figure 21 also shows that the turbulent dissipation rate above the riblets exceeds the value which corresponds to the flow over a smooth surface. By taking into account the data displayed in fig. 20, it appears that an increase in anisotropy results in a decrease in the dissipation rate and that a decrease in anisotropy is associated with an increase in the dissipation rate at the wall. These are fundamental mechanisms of flow control which are relevant for the understanding of turbulent drag reduction.
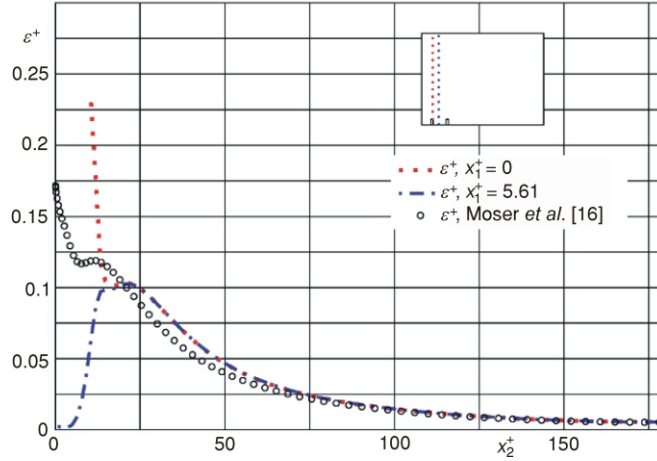
Figure 21. Distributions of the turbulend dissipation rate ε vs. distance from the wall normalized on inner variables in a plane channel flow with smooth walls and in the midplane between the riblet elements

53

The budget of the energy equation presented in fig. 22 reveals that the riblets act to suppress turbulent activity very close to the wall and shift it towards the buffer region. The reduction of the turbulent dissipation rate near the wall is accompanied by a decrease in the turbulent production P_k, which both attain maximum values slightly further away from the wall than in a flat channel. In contrast to flows developing along smooth boundaries in the midplane between the riblets owing to ε_{wall} 0 as x_2 0, the transport term T_k and the viscous diffusion D_k term exhibit similar trends very close to the wall (see fig. 8).

Figure 23 shows the isosurface of the instantaneous vorticity field which visually illuminates a slight reduction in the scale separation between the large scales (L) and

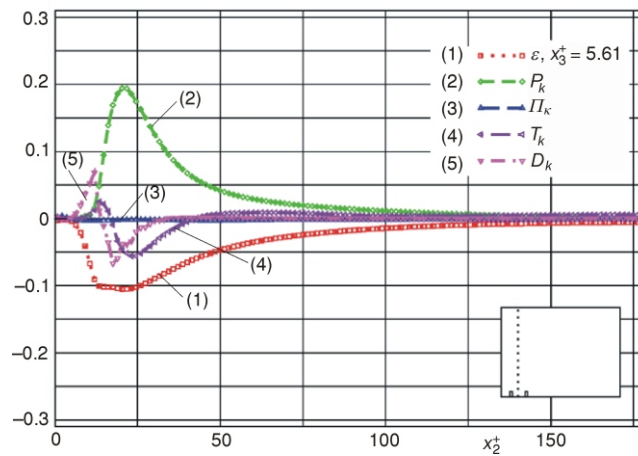**Figure 22. Terms contributing to the balance of the energy k equation scaled on the inner variables for a smooth channel and in the region between the riblet elements**
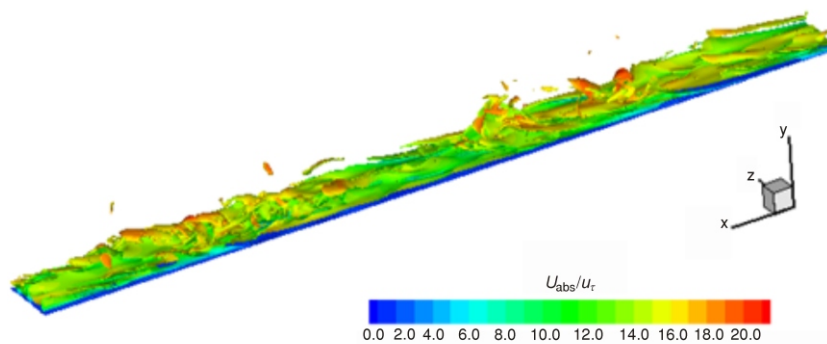

Figure 23. Isosurface of instantaneous vorticity $\left| \vec{U} \right| / (\tilde{u}_\tau^2/\nu)$ 0.4 scaled on the inner variables for a plane channel flow with riblets shown in fig. 5 at Re_t 180 (color image see on our web site)

the small scales (η) in the flow and laminarization of the layer very close to the wall due to action of the riblet elements. In the close vicinity of the wall, turbulent activity is greatly reduced in comparison with the corresponding region of the channel flow with smooth walls shown in fig. 9.

Conclusions

A direct numerical simulation was performed of a plane channel flow, with the two-dimensional roughness elements mounted at the walls and placed perpendicular to the flow. Using the lattice Boltzmann numerical method, all scales were resolved in the computational domain with 1155×129 129 grid points. The numerical results confirm the persistence of turbulence at a Reynolds number of Re   940, based on the centerline velocity and full channel width.

The computed turbulence levels at the channel centerline and in close proximity to the wall were found to be in agreement with typical values for a fully developed turbulent channel flow. The collapse of the mean velocity profiles and the self-similarity of turbulence statistics when scaled on inner variables demonstrate that the simulated flow is controlled entirely by conditions at the wall. Examination of the energy balance suggests that the flow is out of equilibrium and that the production of energy is larger than the viscous dissipation. The computed instantaneous flow fields show the presence of weakly disordered, quasi-periodic structures elongated in the flow direction.

Examination of the simulated data shows that the roughness elements significantly suppress streamwise velocity fluctuations near the wall. Owing to the blockage effect of the roughness elements, the streamwise and the spanwise velocity fluctuations grow at nearly the same rate close to wall. Such behavior of the velocity fluctuations prevents large anisotropy from developing in the near-wall region, which is the essential feature of wall turbulence along smooth boundaries at low Reynolds numbers. Hence the computed results confirm that the chief mechanism responsible for self-maintenance of turbulence at very low Reynolds numbers is related to the reduction of the anisotropy in the velocity fluctuations very close to the wall.

Using the same numerical algorithm, supplementary simulations were performed of a plane channel flow with the riblet elements aligned parallel to the flow direction. Using 4096   257   240 equidistant grids, all scales were resolved within the computation domain, permitting details to be obtained of the chief mechanism associated with turbulence modification by riblets and their influence on the reduction of the wall shear stress.

Numerical results show that riblets with ultra-thin fins and equal finheight to finspacing of about 10 viscous length scales increase the anisotropy of turbulence close to the wall. Anisotropy invariant-mapping of turbulence in the midplane between the riblets revealed that turbulence attains the one-component state at the wall. For such a limiting state of wall turbulence, numerical simulation confirmed that turbulence is damped in close proximity of the wall by suppression of the lateral velocity fluctuations which are constrained to follow the same trend as the fluctuations perpendicular to the

wall. In addition the turbulent dissipation rate is forced to vanish at the solid surface and significant reduction of the wall shear stress occur which overweight the reduction of the wall shear stress if the flow assumed a laminar state. Hence the simulated results confirm that the chief mechanism responsible for reduction of the wall shear stress is associated with an increase in the anisotropy of turbulence in the region very close to the wall.

Acknowledgments

Appendix

Transition and breakdown to turbulence induced by small axisymmetric disturbances developing in a laminar, flat plate boundary layer

Starting from the Navier-Stokes and continuity equations for a viscous incompressible fluid:

$$\frac{\partial u_i}{\partial t} + u_k \frac{\partial u_i}{\partial x_k} = -\frac{1}{\rho}\frac{\partial p}{\partial x_i} + \nu \frac{\partial^2 u_i}{\partial x_k \partial x_k}, \quad \frac{\partial u_k}{\partial x_k} = 0, \quad i,k = 1,2,3 \tag{16}$$

and introducing the conventional method of separating the instantaneous velocity u_i and the pressure p into the mean-laminar flow and the disturbances u_i and p superimposed on it:

$$u_i = U_i + u_i, \quad p = P + p \tag{17}$$

one obtains the equations for the disturbances:

$$\frac{\partial u_i}{\partial t} + U_k \frac{\partial u_i}{\partial x_k} + u_k \frac{\partial U_i}{\partial x_k} = -\frac{1}{\rho}\frac{\partial p}{\partial x_i} + \nu \frac{\partial^2 u_i}{\partial x_k \partial x_k}, \quad \frac{\partial u_k}{\partial x_k} = 0 \tag{18}$$

In the derivation of the above equations, it is assumed that the disturbances are much smaller than the corresponding quantities of the mean flow:

$$u_i \ll U_i, \quad p \ll P \tag{19}$$

and that they satisfy the Navier-Stokes and the continuity equations.

If we consider the disturbances to be random, then by systematic manipulation of eq. (18) it is possible to obtain transport equations for the "apparent" stresses (see, for example [41]):

$$\frac{\partial \overline{u_i u_j}}{\partial t} \quad U_k \frac{\partial \overline{u_i u_j}}{\partial x_k}$$

$$\underbrace{\overline{u_j u_k} \frac{\partial U_i}{\partial x_k} \quad \overline{u_i u_k} \frac{\partial U_j}{\partial x_k}}_{P_{ij}} \quad \underbrace{\frac{1}{\rho} \overline{u_j \frac{\partial p}{\partial x_i}} \quad \overline{u_i \frac{\partial p}{\partial x_j}}}_{\Pi_{ij}} \quad \underbrace{2\nu \overline{\frac{\partial u_i}{\partial x_k} \frac{\partial u_j}{\partial x_k}}}_{\varepsilon_{ij}} \quad \nu \frac{\partial^2 \overline{u_i u_j}}{\partial x_k \partial_k} \tag{20}$$

In the above equations, one can identify two different types of unknown correlations: the velocity-pressure gradient correlations (Π_{ij}) and the dissipation correlations (ε_{ij}). These correlations must be expressed in terms of U_i and $\overline{u_i u_j}$ in order to close the resultant eq. (20) for the apparent stresses.

To illuminate the statistical dynamics of the apparent stresses during the laminar-turbulent transition process, we may utilize the closure proposals for ε_{ij} and Π_{ij} elaborated in detail by Jovanović [19]. Using the two-point correlation technique and the invariant theory, he suggested the following approximations for the unknown terms in the transport equations for the apparent stresses:

$$\varepsilon_{ij} \quad \frac{1}{4} \nu \frac{\partial^2 \overline{u_i u_j}}{\partial x_k \partial x_k} \quad \mathcal{A} \varepsilon_h a_{ij} \quad \frac{1}{3} \varepsilon_h \tag{21}$$

and

$$\Pi_{ij} \quad a_{ij} P_{ss} \quad \mathcal{F} \quad \frac{1}{3} P_{ss} \delta_{ij} \quad P_{ij} \quad \text{small transport terms} \tag{22}$$

Here $\mathcal{A}$ and $\mathcal{F}$ are scalar functions that depend on the anisotropy invariants and the Reynolds number based on the Taylor microscale, $\mathrm{Re}_\lambda = \lambda q/\nu$, and $\varepsilon_h = 5\nu q^2/\lambda^2$ is the homogeneous part of the dissipation rate [19]:

$$\varepsilon \quad \frac{1}{4} \nu \frac{\partial^2 q^2}{\partial x_k \partial x_k} \quad \varepsilon_h \tag{23}$$

The above closure proposals satisfy the two-component limit and therefore realizability, coincide with the exact solutions available for vanishing anisotropy in the disturbances, behave properly for low and large Reynolds numbers and reduce to an appropriate tensorial form for the axisymmetric disturbances.

Using the suggested forms for ε_{ij} and Π_{ij}, the transport equations for the apparent stresses may be written in the closed form:

$$\frac{\partial \overline{u_i u_j}}{\partial t} \quad U_k \frac{\partial \overline{u_i u_j}}{\partial x_k}$$

$$P_{ij} \quad a_{ij} P_{ss} \quad \mathcal{F} \quad \frac{1}{3} P_{ss} \delta_{ij} \quad P_{ij} \quad 2\mathcal{A} \varepsilon_h a_{ij} \quad \frac{2}{3} \varepsilon_h \delta_{ij} \quad \frac{1}{2} \nu \frac{\partial^2 \overline{u_i u_j}}{\partial x_k \partial x_k} \qquad (24)$$

We may follow the same analytical path for the treatment of the transport equation for the homogeneous part of the dissipation rate ε_h. After lengthly derivations, which were elaborated by Jovanović [19], the following equation emerges in a closed form:

$$\frac{\partial \varepsilon_h}{\partial t} \quad U_k \frac{\partial \varepsilon_h}{\partial x_k} \quad 2\mathcal{A} \frac{\varepsilon_h \overline{u_i u_k}}{k} \frac{\partial U_i}{\partial x_k} \quad \psi \frac{\varepsilon_h^2}{k} \quad \frac{1}{2} \nu \frac{\partial^2 \varepsilon_h}{\partial x_k \partial x_k} \qquad (25)$$

Here ψ is another scalar function which also depends on the anisotropy invariants and the Reynolds number Re_λ.

Contraction of the transport equations for the apparent stresses, eq. (20), yields the energy equation $(k = q^2/2)$ for the disturbances:

$$\frac{\partial k}{\partial t} \quad U_k \frac{\partial k}{\partial x_k} \quad P_k \quad \varepsilon_h \quad \frac{1}{2} \nu \frac{\partial^2 k}{\partial x_k \partial x_k} \qquad (26)$$

If we consider transition of the flow in a flat plate boundary layer, then the energy equation immediately suggests stability towards small disturbances if the production is balanced by the dissipation:

$$P_k \quad \varepsilon_h \qquad (27)$$

The equilibrium constraint leads to the equation for the energy:

$$\frac{\partial k}{\partial t} \quad U_k \frac{\partial k}{\partial x_k} \quad \frac{1}{2} \nu \frac{\partial^2 k}{\partial x_k \partial x_k} \qquad (28)$$

which is of boundary layer character and does not allow amplification of statistically stationary disturbances in the boundary layer [42].

Inserting the equilibrium constraint $P_k \quad \varepsilon_h$ into the dissipation rate equation:

$$\frac{\partial \varepsilon_h}{\partial t} \quad U_k \frac{\partial \varepsilon_h}{\partial x_k} \quad \underbrace{(2\mathcal{A} \quad \psi)}_{\substack{0 \\ \text{to insure} \\ \text{that } \varepsilon_h \ 0}} \frac{\varepsilon_h^2}{k} \quad \frac{1}{2} \nu \frac{\partial^2 \varepsilon_h}{\partial x_k \partial x_k} \qquad (29)$$

and specifying that the dissipation rate is always positive, $\varepsilon_h \quad 0$, we deduce the transition criterion in terms of the Reynolds number based on the intensity (q^2), the length scale (λ) and the anisotropy $(\mathrm{II}_a, \mathrm{III}_a)$ of the disturbances as follows:

$$2\mathcal{A} - \psi = 0 \qquad (30)$$

58

For a certain magnitude (II_a) and character (III_a) of the anisotropy in the disturbances, the derived transition criterion (30) suggests the permissible magnitudes for the intensity and the length scale of disturbances Re_λ $(Re_\lambda)_{crit}$ that guarantee balance (27) (P_k ε_h with ε_h 0) and therefore maintenance of the laminar flow regime in a flat plate boundary layer.

The transition criterion is determined from the requirement that the laminar boundary layer should be neutrally stable to small, statistically stationary axisymmetric disturbances, which is equivalent to the local (and therefore also global) equilibrium discussed. As a consequence of this requirement, the energy k cannot grow in the boundary layer above corresponding values of the free stream. However, this conclusion does not hold for the scale λ, which must follow increases in the shear layer thickness (λ δ) as it develops downstream. This behavior of q^2 and λ implies that the dissipation rate $\varepsilon_h = 5\nu q^2/\lambda^2$ will decrease with increasing Reynolds number until it reaches some minimum value required by the dissipation rate equation to induce transition and breakdown to turbulence.

Using expressions for the scalar functions $\mathcal{A}$ and ψ constructed analytically by Jovanović, Otić, and Bradshaw [43]:

$$\mathcal{A} \quad \begin{cases} 1 \quad 1 \quad 9\frac{1}{2}II_a \quad \frac{3}{4}\sqrt{\frac{2}{3}II_a}^{\,3} & (W \quad 1), \quad III_a \quad 0 \\[2em] 1 \quad 1 \quad 9\frac{1}{2}II_a \quad \frac{3}{4}\sqrt{\frac{2}{3}II_a}^{\,3} & (W \quad 1), \quad III_a \quad 0 \end{cases} \tag{31}$$

$$\psi \quad \begin{cases} 1 \quad 9\frac{1}{2}II_a \quad \frac{3}{4}\sqrt{\frac{2}{3}II_a}^{\,3} \quad (1.8 \quad 0.4W), & III_a \quad 0 \\[2em] 22.5 \quad \frac{1}{2}II_a \quad \frac{3}{4}\sqrt{\frac{2}{3}II_a}^{\,3} \quad 1 \quad 9\frac{1}{2}II_a \quad \frac{3}{4}\sqrt{\frac{2}{3}II_a}^{\,3} \quad (1.8 \quad 0.4W), \quad III_a \quad 0 \end{cases} \tag{32}$$

with

$$W \quad 0.0306\,Re_\lambda \quad 0.313\sqrt{0.009604\,Re_\lambda^2 \quad 10208} \tag{33}$$

it is easy to prove from criterion (30) that for $III_a > 0$, $(II_a)_{wall} = 2/9$, and $(II_a)_\infty$ 0.15 the laminar regime in a flat plate boundary layer will remain up to infinite Reynolds numbers. For $III_a < 0$ and $(II_a)_{wall} = 1/6$ the transition criterion (30) cannot be satisfied for any value of R_λ and therefore we expect that for such disturbances turbulence will appear in the boundary layer at very low Reynolds numbers. These analytical results corresponding to two different modes of the axisymmetric disturbances are displayed in

fig. 1. This figure suggests that the most effective way to initiate and maintain turbulence at very low Reynolds number is to reduce the anisotropy in the disturbances close to the wall to a minimum by forcing these to tend towards the isotropic two-component limit at the wall.

Reference

[1] Deardorff, J. W., A Numerical Study of Three-Dimensional Turbulent Channel Flow at Large Reynolds Numbers, *J. Fluid Mech.*, *41* (1970), pp. 453-480

[2] Orszag, S. A., Patterson, G. S., Numerical Simulation of Three-Dimensional Homogeneous Isotropic Turbulence, *Phys. Rev. Lett.*, *28* (1972), pp. 76-79

[3] Schumann, U., A Method for Direct Numerical Simulaion of Turbulence in Plane and Annular Channels and Its Application for Development of Turbulence Models (in German), Ph. D. thesis, Universität Karlsruhe, Karlsruhe, Germany, 1973

[4] Rogallo, R. S., Numerical Experiments in Homogeneous Turbulence, NASA Tech. Memo 81315, USA, 1981

[5] Kim, J., Moin, P., Moser, R., Turbulence Statistics in Fully Developed Channel Flow at Low Reynolds Number, *J. Fluid Mech.*, *177* (1987), pp. 133-166

[6] Spalart, P. R., Numerical Study of Sink-Flow Boundary Layers, *J. Fluid Mech.*, *172* (1986), pp. 307-328

[7] Spalart, P. R., Direct Simulation of a Turbulent Boundary Layer up to $Re_\theta = 1410$, *J. Fluid Mech.*, *187* (1988), pp. 61-98

[8] Gilbert, N., Kleiser, L., Turbulence Model Testing with the Aid of Direct Numerical Simulation Results, *Proceedings*, Eighth Symposium on Turbulent Shear Flows, Munich, Germany, 1991, pp. 26.1.1-26.1.6

[9] Lyons, S. L., Hanratty, T. J., McLaughlin, J. B., Large-Scale Computer Simulation of Fully Developed Turbulent Channel Flow with Heat Transfer, *Int. J. Numer. Met. Fluids, 13* (1991), pp. 999-1028

[10] Antonia, R. A., Teitel, M., Kim, J., Browne, L.W. B., Low-Reynolds-Number Effects in a Fully Developed Turbulent Channel Flow, *J. Fluid Mech.*, *236* (1992), pp.579-605

[11] Kuroda, A., Kasagi, N., Hirata, M., Direct Numerical Simulation of the Turbulent Plane Couette-Poiseulle Flows: Effect of the Mean Shear on the Near Wall Turbulent Structures, *Proceedings*, Ninth Symposium on Turbulent Shear Flows, Kyoto, Japan, 1993, pp. 241-257

[12] Eggels, J., Unger, F., Weiss, M. Westerweel, H., J., Adrian, R. J., Friedrich, R., Nieustadt, F. T. M., Fully Developed Turbulent Pipe Flow: a Comparison between Direct Numerical Simulation and Experiment., *J. Fluid Mech.*, *268* (1994), pp.175-209

[13] Choi, H., Moin, P., Kim, J., Direct Numerical Simulation of Turbulent Flow Over Riblets, *J. Fluid Mech.*, *255* (1993), pp. 503-539

[14] Le, H., Moin, P., Direct Numerical Simulation of Turbulent Flow over a BackWard-Facing Step, Thermoscience Division Dep. Mech. Eng. Rep. TF-58, 1994, Stanford University, USA

[15] Rogers, M. M., Moser, R. D., Direct Simulation of a Self-Similar Turbulent Mixing Layer, *Phys. Fluids*, *6* (1994), pp. 903-923

[16] Moser, R., Kim, J., Mansour, N., Direct Numerical Simulation of Turbulent Channel Flow up to $Re_\tau = 560$, *Phys. Fluids, 11* (1999), pp. 943-945

[17] Reynolds, O., On the Dynamical Theory of Incompressible Viscous Fluids and the Determination of the Criterion, *Phil. Trans. R. Soc. Lond. A*, *186* (1895), pp. 123-164

[18] Taylor, G. I., Statistical Theory of Turbulence, Part V. Effects of Turbulence on Boundary Layer. Theoretical Discussion of Relationship between Scale of Turbulence and Critical Resistance of Spheres, *Proc. R. Soc. Lond. A*, *156* (1936), pp. 307-317

[19] Jovanović, J., The Statistical Dynamics of Turbulence, Springer-Verlag, Berlin, 2004

[20] Jovanović, J., Pashtrapanska, M., On the Criterion for the Determination Transition Onset and Breakdown to Turbulence in Wall-Bounded Flows, *J. Fluids Eng.*, *126* (2004), pp. 626-633

[21] Lumley, J. L., Newman, G., The Return to Isotropy of Homogeneous Turbulence, *J. Fluid Mech., 82* (1977), pp. 161-178

[22] Lumley, J. L., Computational Modeling of Turbulent Flows, *Adv. Appl. Mech.*, *18* (1978), pp. 123-176

[23] Jovanović, J., Hillerbrand, R., Pashtrapanska, M., The Statistical Analysis of the Origin of Turbulence Using Numerical Databases (in German), *KONWIHR Quartl 31* (2001), pp. 6-8

[24] Jovanović, J., Frohnapfel, B., Skaljić, E., Jovanović, M., Persistence of the Laminar Regime in a Flat Plate Boundary Layer at Very High Reynolds Number, *Thermal Science, 10* (2006), 2, pp. 63-96 (in this issue)

[25] Jovičić, N., Breuer, M., Separated Flow Past an Airfoil at High Angle of Attack: Les Predictions and Analysis, 5th Workshop on DNS & LDES, Munich, Germany, 2003, ERCOFTAC Series, Vol. 9, pp. 611-618, DNS and LES V (Eds. R. Friedrich *et al.*), Kluwer Acad. Publ., Dordrecht, The Netherlands

[26] Jovanović, J., Hillerbrand, R., On Peculiar Property of the Velocity Fluctuations in Wall-Bounded Flows, *Thermal Science, 9* (2005), 1 pp. 3-12

[27] Jovanović, J., Pashtrapanska, M., Frohnapfel, B., Durst, F., Koskinen, J., Koskinen, K., On the Mechanism Responsible for Turbulent Drag Reduction by Dilute Addition of High Polymers: Theory, Experiments, Simulations and Predictions, *J. Fluids Eng*. *128* (2006), pp. 118-130

[28] Benzi, R., Succi, S., Vergassola, M., The Lattice Boltzmann Equation: Theory and Applications, *Physics Reports (Review Section of Physics Letters)*, *222* (1992), pp. 145-197

[29] Chen, S., Doolen, G. D., Lattice Boltzmann Method for Fluid Flows, *Annu. Rev. Fluid Mech.*, *30* (1998), pp. 329-364

[30] Wolf-Gladrow, D. A., Lattice-Gas Cellular Automata and Lattice Boltzmann Models. Springer-Verlag, Berlin, 2000

[31] Succi, S., The Lattice Boltzmann Equation – For Fluid Dynamics and Beyond, Clarendon Press, Oxford, UK, 2001

[32] Bhatnagar, P., Gross, E. P., Krook, M. K., A Model for Collision Processes in Gases, I. Small Amplitude Processes in Charged and Neutral One-Component Systems, *Phys. Rev.*, *94* (1954), pp. 511-525

[33] Hou, S., Zou, Q., Chen, S., Doolen, G., Cogley, A. C., Simulation of Cavity Flow by the Lattice Boltzmann Method, *J. Comput. Phys., 118* (1995), pp. 329-347

[34] Buick, J., Greated, C., Gravity in Lattice Boltzmann Model, *Phys. Rev. E*, *61* (2000), pp. 5307-5320

[35] He, X., Luo, L.-S., Theory of the Lattice Boltzmann Method: from the Boltzmann Equation to the Lattice Boltzmann Equation, *Phys. Rev. E*, 56 (1997), pp. 6811-6817

[36] Chapman, S., Cowling, T. G., The Mathematical Theory of Non-Uniform Gases, Cambridge University Press, Cambridge, UK, 1999

[37] Qian, Y. H., d'Humieres, D., Lallemand, P., Lattice BGK Models for Navier-Stokes Equation, *Europhys. Lett.*, *17* (1992), pp. 479-484

[38] He, X., Zou, Q., Luo, L.-S., Dembo, M., Analytic Solutions of Simple Flows and Analysis of Nonslip Boundary Conditions for the Lattice Boltzmann BGK Model. *J. Stat. Phys.*, *87* (1997), pp. 115-136

[39] Zeiser, T., Steven, M., Freund, H., Lammers, P., Brenner, G., Durst, F., Bernsdorf, J., Analysis of the Flow Field and Pressure Drop in Fixed Bed Reactors with the Help of Lattice Boltzmann Simulations, *Phil. Trans. R. Soc. Lond. A*, *360* (2002), pp. 507-520

[40] Fischer, M., Jovanović, J., Durst, F., Reynolds Number Effects in the Near-Wall Region of Turbulent Channel Flows, *Phys. Fluids*, *13* (2001), pp. 1755-1767

[41] Hinze, J. O., Turbulence, 2nd ed., McGraw-Hill, New York, USA, 1975

[42] Schlichting, H., Boundary-Layer Theory, 6th ed., McGraw-Hill, New York, USA, 1968

[43] Jovanović, J., Otić, I., Bradshaw, P., On the Anisotropy of Axisymmetric Strained Turbulence in the Dissipation Range, *J. Fluids Eng.*, *125* (2003), pp. 401-413

Authors' address:

P. Lammers, J. Jovanović, F. Durst
Lehrstuhl für Strömungsmechanik
Universität Erlangen-Nürnberg
Cauerstrasse 4, 91058 Erlangen, Germany